Title
Chapter Twelve Cryo-EM studies of NAIP–NLRC4 inflammasomes

Permalink
https://escholarship.org/uc/item/3nr5p4cv

Authors
Haloupek, Nicole
Grob, Patricia
Tenthorey, Jeannette
et al.

Publication Date
2019

DOI
10.1016/bs.mie.2019.04.030

Peer reviewed

Cryo-EM studies of NAIP–NLRC4 inflammasomes

Nicole Haloupek[a,*], **Patricia Grob**[b], **Jeannette Tenthorey**[a,†], **Russell E. Vance**[a,b], **Eva Nogales**[a,b,c,*]

[a]Department of Molecular and Cell Biology, UC Berkeley, Berkeley, CA, United States

[b]Howard Hughes Medical Institute, UC Berkeley, Berkeley, CA, United States

[c]Molecular Biophysics and Integrated Bioimaging Division, Lawrence Berkeley National Lab, Berkeley, CA, United States

Abstract

The NAIP–NLRC4 family of inflammasomes are components of the innate immune system that sound a molecular alarm in the presence of intracellular pathogens. In this chapter, we provide an in-depth guide to using cryo-electron microscopy (cryo-EM) to investigate these inflammasomes, focusing especially on the techniques we used in our recent structural analysis of the NAIP5–NLRC4 inflammasome. We explain how to circumvent specific obstacles we encountered at each step, from sample preparation through data processing. The methods described here will be useful for further studies of the NAIP5–NLRC4 inflammasome and related supracomplexes involved in innate immune surveillance; they may also be useful for unrelated complexes that present similar issues, such as preferential orientations and compositional heterogeneity.

1. Introduction

NAIP–NLRC4 inflammasomes are protein complexes composed of a single NAIP (NLR family, apoptosis inhibitory protein) bound to a variable number of NLRC4 (NLR family, CARD [Caspase Activation and Recruitment Domain]-containing 4) subunits. Their role in the innate immune system is to detect the presence of intracellular pathogens and initiate a signaling cascade leading to pyroptosis, a form of programmed cell death that causes inflammation, and inflammatory cytokine release that initiates an immune response to restrict the proliferation of the pathogen (Bergsbaken, Fink, & Cookson, 2009; Jones, Vance, & Dangl, 2016).

The open-ring-shaped structures assumed by these inflammasomes are nucleated by a bacterial ligand bound to a NAIP, with the ligand preference being dictated by the specific NAIP isoform that is engaged. NAIP5, the sensor on which this chapter will primarily focus, detects the bacterial protein flagellin, whereas its paralogs NAIP1 and NAIP2 detect the needle and inner rod proteins, respectively, of bacterial type III secretion systems (Kofoed & Vance, 2011; Rayamajhi, Zak, Chavarria-Smith, Vance, & Miao, 2013; Yang, Zhao, Shi, &

[*]Corresponding authors: nhaloupek@gmail.com; enogales@lbl.gov.
[†]Present address: Basic Sciences Division, Fred Hutchinson Cancer Research Center, Seattle, WA, United States.

Shao, 2013; Zhao et al., 2011). Other than detecting different ligands, these inflammasomes appear to work in similar ways.

Structural studies have uncovered much information about the mechanism of inflammasome formation and activation, from revealing how NAIPs bind their ligands to hinting how, once assembled, inflammasomes exert their effects. Ligand binding by a NAIP and the consequent inflammasome formation are only the first steps in a larger pathway. Structural and biochemical work has shown that the CARD of NLRC4 binds procaspase-1, juxtaposing the proenzymes within the oligomeric complex to facilitate their dimerization and maturation into active caspase-1 (Lu et al., 2016; Shi, 2004). The active caspase-1 then cleaves the inflammatory cytokines pro-interleukin-1β and pro-interleukin-18 into their mature forms (Broz & Dixit, 2016; Martinon, Burns, & Tschopp, 2002). Caspase-1 also cleaves gasdermin D, the N-terminal portion of which forms pores in the plasma membrane, triggering the release of mature cytokines and pyroptosis (Aglietti et al., 2016; Chen et al., 2016; Ding et al., 2016; Liu et al., 2016; Ruan, Xia, Liu, Lieberman, & Wu, 2018; Sborgi et al., 2016).

Recently, we published the complete structure of the flagellin-bound NAIP5–NLRC4 inflammasome as well as a partial inflammasome structure consisting of NAIP5 bound to flagellin and two NLRC4 subunits at a higher overall resolution of 5.2 Å (Tenthorey et al., 2017). Shortly thereafter, Yang et al. reported the structure of NAIP5 bound to the NAIP5-activating portion of flagellin and one NLRC4 subunit at 4.3 Å resolution (Yang et al., 2017). Because the two published structures contained slightly different components and were obtained in different ways, as we will explain at later points in this chapter, they should be considered complementary to one another. There is likely room for improvements in resolution for these structures, especially in regions where the resolution of both structures suffered due to flexibility, such as the NAIP5 BIR (baculovirus inhibitor-of-apoptosis repeat) domains, where some conflict in the modeling of the structures exists between the two studies.

In this chapter, we will give a detailed description of our methods, focusing on less conventional technical aspects that were designed by our group specifically for work on the NAIP5–NLRC4 inflammasome. We also provide suggestions that may help future researchers improve on what we and others have done so far in the study of inflammasomes and other challenging samples being studied by cryo-EM.

2. Preparing NAIP–NLRC4 inflammasomes for EM

Cryo-electron microscopy (cryo-EM) has generally been the method of choice for structural studies of inflammasomes. The structure of inactive NLRC4 lacking its CARD has been solved using X-ray crystallography (Hu et al., 2013), but full inflammasome complexes do not seem amenable to crystallographic studies. First, it has not been possible, in our experience, to produce enough of these complexes for systematic crystallization trials. Second, inflammasomes are constitutionally heterogeneous (containing variable numbers of NLRC4 subunits) and conformationally heterogeneous, characteristics that do not typically bode well for crystallography.

The cryo-electron microscopist has many tools for dealing with such heterogeneity; however, it can still pose a significant challenge. In our cryo-EM studies of the NAIP5–NLRC4 inflammasome, we also encountered other difficulties, including sample sensitivity to the air–water interface, preferred orientations of the inflammasomes on EM grids, and low numbers of particles per micrograph. In this section, we describe these issues in further detail. In Sections 3–5 of this chapter, we present solutions to these problems, many of which may also be applicable to other, unrelated complexes, and provide in-depth explanations of our group's protocols so that they may be replicated and, we hope, improved upon.

2.1 Heterogeneity-related obstacles

Garnering structural information about inflammasomes has not proven trivial. The constitutional and conformational heterogeneity that in part limit the use of crystallography in studying these inflammasomes are also problematic—although not intractably so—in cryo-EM studies. Cryo-EM relies on averaging two-dimensional projections of individual molecules (particles) to achieve high-resolution structures. We have observed that NAIP5–NLRC4 inflammasomes tend to exhibit CARD-mediated ring stacking in solution, and that this stacking is haphazard, leading to a variety of conformations that complicate averaging and severely restrict resolution. Not only does the stacking limit resolution, but we also believe the stacked rings are unlikely to be a biologically relevant form of the complex, since stacking occludes the CARDs of NLRC4, which are necessary for interaction with (and, thus, activation of) procaspase-1.

2.2 Sensitivity to the air–water interface and preferred orientations

NAIP–NLRC4 inflammasomes also appear highly sensitive to the air–water interface, posing a particular problem for cryo-EM studies. In cryo-EM, thinner ice generally yields structures of higher resolution because buffer components scatter electrons, blurring particle images in areas where ice is thick. However, very thin ice is not suitable for studying NAIP–NLRC4 inflammasomes because they are large, disk-shaped complexes, so ice that is somewhat thicker than what is usually desirable for cryo-EM is needed to obtain projections of the side views of the complexes. Therefore, a careful balance must be struck to obtain ice that is as thin as possible to support high-resolution reconstructions while also being just thick enough to support the side views. NAIP5–NLRC4 inflammasome grids with ice that is too thin are easy to recognize under the electron microscope: side views will be confined to the edges of holes (where the ice is typically thicker) or will simply not be seen at all.

2.3 Low particle number

Additionally, simply getting inflammasomes to adhere to EM grids proved problematic in our studies. Incubating sample droplets on the grids for longer periods of time than are often used increases the particle concentration, but in our experiments, water evaporation from the sample droplet limited our incubation time, even when incubation was done in a humidity chamber. We have found that over longer incubation periods, the inflammasomes degraded into indistinct "exploded" particles, likely due to exposure to the air-water interface, especially as the water evaporates.

3. Biochemical preparation

The first step toward obtaining any high-resolution structure using cryo-EM is to biochemically optimize the sample. Despite the fact that improved methods for particle picking and sorting are continuously being developed, sample impurities can lead to reduced resolution, inaccuracies, or, at worst, failure to obtain a structure at all. Concentration is also a concern; if the concentration is too low and few particles adhere to the EM grid, it is difficult to collect enough particle images to enable high-resolution reconstructions.

To achieve high yield and concentration for our inflammasome preparations, we experimented with several heterologous expression systems, including insect and mammalian cells. We found that co-expression of inflammasome components in HEK-293T cells achieved sufficient yields; this system also had the advantage of recapitulating the known biological properties of NAIP–NLRC4 inflammasomes (Kofoed & Vance, 2011).

To achieve sufficient purity, we isolated inflammasomes from these cells using a two-step purification protocol. We first immuno-affinity purified NAIP5 using an N-terminal FLAG tag and commercially available resin containing a highly specific anti-FLAG antibody. In principle, this purification should yield a mixture of monomeric NAIP5, NAIP5 bound to its ligand fagellin, and a mixture of partially or fully assembled NAIP5–NLRC4 inflammasomes. To separate the fully assembled complexes, we subjected our FLAG-purified NAIP5 to size-exclusion chromatography, which separates proteins based on their hydrodynamic radius (roughly, size). This allowed us to isolate large (>1 MDa) protein complexes that, as assessed by Western blot, contained NAIP5, fagellin, and a stoichiometric excess of NLRC4.

For the reasons previously discussed, with respect to both heterogeneity (mainly concerning ring stacking) and concentration, the biochemical preparation of NAIP–NLRC4 inflammasomes requires care. Further, these inflammasomes contain flexible elements, which hamper efforts to achieve high resolution if not managed. In this section, we discuss methods for mitigating these problems, some of which may be applicable to other complexes being studied using cryo-EM, and provide our protocol for the biochemical preparation of NAIP5–NLRC4 inflammasomes.

3.1 Preventing constitutional heterogeneity

As previously discussed, the tendency of NAIP–NLRC4 inflammasome rings to stack is a major problem for EM studies, and each group studying these complexes using cryo-EM has taken a different approach to addressing it.

In one structural study, Hu et al. used a truncated NLRC4 lacking the stacking-mediating CARD (NLRC4 [CARD]), thus completely eliminating the problem (Hu et al., 2015). Using radial averaging, the group was able to determine the structure of active NLRC4 [CARD] at high resolution, revealing that the global conformation of NLRC4 [CARD] in assembled inflammasomes (as observed in vitreous ice in cryo-EM) differs from the previously published structure of crystallized monomeric NLRC4 [CARD]. Because of the radial averaging, they were not able to solve the structure of the NAIP or its ligand as these

proteins were each present in only one copy per ring and the average was thus dominated by NLRC4.

Deleting the CARD is only one option for preventing ring stacking, and it does have drawbacks. The most obvious of these is that CARD deletion makes it impossible to visualize the CARDs. However, despite not deleting the CARDs, our group and others have not been able to attain inflammasome structures with high resolution in the CARD region, possibly because of flexibility between the CARDs and the rest of the structure or inherent flexibility within the CARDs themselves as they exist in the inflammasome structure. Other drawbacks of deleting the CARDs are that it is conceivable that the same structure would not form in the presence of CARDs and that it would not be possible to perform structural studies of the inflammasomes with their partner, caspase-1, the binding of which is mediated by the CARDs.

Instead of using NLRC4 ^{CARD}, our group used NLRC4 with an N-terminal green fluorescent protein (GFP) linked to the CARDs to sterically block CARD–CARD interactions (Tenthorey et al., 2017). This reduced but did not fully prevent ring stacking. With the addition of two targeted mutations in the CARD (F79A and D83A) aimed at preventing stacking based on what was known about the CARD–CARD interface, we observed that stacking was nearly completely eliminated (see Fig. 1). We note that the introduction of these CARD mutations prevents recruitment of caspase-1 by the CARDs, so future attempts to visualize the entire flagellin–NAIP–NLRC4–caspase-1 holocomplex will need to rely on non-mutated NLRC4.

A further source of heterogeneity in NAIP–NLRC4 inflammasome preparations is the number of NLRC4 subunits each ring contains. While we ultimately dealt with this computationally (see Section 5.2), another strategy, employed by Yang et al., is to prevent full rings from forming by mutating the NLRC4 oligomerization "donor" surface such that while NLRC4 can still be recruited to NAIP, NLRC4 cannot recruit additional NLRC4 protomers (Yang et al., 2017). These are only two possible options, and it is conceivable that future studies will include better ways of dealing with the constitutional heterogeneity observed with these inflammasomes.

Note that we did attempt to reduce the problem of heterogeneity of NAIP5–NLRC4 inflammasomes due to different number of NLRC4 molecules by crosslinking the sample with glutaraldehyde prior to grid application. This produced no noticeable improvement in our results, leading us to use computational methods to deal with the heterogeneity instead (see Section 5). However, it may be worth attempting to stabilize the complex with other crosslinkers in future studies.

3.2 Preventing conformational heterogeneity

In addition to compositional heterogeneity, we have observed that some parts of the NAIP5–NLRC4 inflammasome exhibit marked conformational heterogeneity. The NLRC4 CARD, in particular, has never been a well-resolved domain in any of our inflammasome structures, instead appearing as a blurry density at the center of the ring. We attempted adding caspase-1 to inflammasomes prepared with wild-type GFP-NLRC4 in the hope that it might

stabilize the CARDs, but this did not improve resolution in the CARD region in our preliminary tests. Still, we believe the caspase-1-bound inflammasome may be an interesting structural target on its own and is worth pursuing in further studies.

Another apparently flexible region is the large portion of flagellin that does not bind NAIP5. One solution to this problem is to use truncated flagellin containing only the NAIP5–binding domain, which was the strategy employed by Yang et al. (2017). We opted to use full-length fagellin, which allowed us to visualize slightly more of the subunit at a cost to overall resolution (Tenthorey et al., 2017). Areas in the N-terminal region of NAIP5, including the three BIR domains and the linkers connecting them, also appear relatively flexible. This is particularly troublesome since the BIRs are very similar to one another, making unambiguous assignment of each one to a portion of the density a challenge.

3.3   Protocol for biochemical preparation of NAIP5–NLRC4 inflammasomes

3.3.1   Equipment

- CO_2 incubator set to 37 °C and humidified with sterile water

- Biosafety cabinet

- Light microscope, GFP laser optional

- Centrifuge, preferably one that allows chilling

- Microcentrifuge that allows chilling (or one used in cold room)

- Tube rotator (in cold room)

- High performance liquid chromatography (HPLC) system (in cold room or deli case refrigerator)

- Superose6 10/300 GL size exclusion column

3.3.2   Materials

- HEK293T cells or other easily transfected cell line

- DMEM (Gibco)

- Fetal bovine serum (Gibco)

- 200 mM L-glutamine (Gibco)

- 10,000 U/mL Penicillin/Streptomycin (Gibco)

- Phosphate-buffered saline, pH 7.4 (Gibco)

- Trypsin-EDTA (Gibco)

- Tissue culture-treated plates

- Sterile serological pipettes

- Sterile Pasteur pipettes

- Cell scraper

- Lipofectamine 2000 (Invitrogen)

- Optimem (Gibco)

- GFP-NLRC4-F79A/D83A, FLAG-NAIP5, and 6myc-FlaA plasmids, purified from *E. coli* using a midiprep or maxiprep kit

- 15- and 50-mL conical tubes

- Eppendorf tubes

- HEPES, pH 7.6

- NaCl

- KCl

- $MgCl_2$

- Glycerol

- Triton X-100

- NP-40

- DTT

- Trehalose

- 100mM glycine, pH 3.5

- NaN_3 (optional)

- Protease inhibitor tablets (Roche)

- FLAG M2 agarose resin (Sigma)

- FLAG peptide (Sigma)

- 10 mL chromatography column, with top cap and stopcock

- Ring stand with column clamp

- 500mL 0.2 μm filter

- HPLC loading needle

- 1 mL HPLC sample loop

- HPLC manual injection syringe

3.3.3 Protocol

1. Grow HEK293T cells on sterile, tissue culture-treated plates in DMEM supplemented with 10% fetal bovine serum (FBS), 2 mM L-glutamine, and 100U/mL penicillin/streptomycin. These cells double in number roughly every 24 h, and should be passaged when they reach confluency (i.e., when they cover most of the plate's surface area). To passage cells, aspirate the media, gently rinse with PBS, aspirate PBS, incubate in trypsin at 37 °C for several minutes, and resuspend in supplemented DMEM. Cells can then be pelleted, resuspended

in fresh media, and diluted up to 10-fold for further growth in fresh plates. Cells are grown in a humidified CO_2 incubator at 37 °C and are handled exclusively in a biosafety cabinet.

2. Prepare HEK293T for expressing inflammasome components by harvesting confluent plates and re-plating in 15-cm plates at a 1:4 dilution 1 day prior to transfection. Typically, 6–12 plates are required for sufficient yield. Cells should be roughly 50% confluent the following day.

3. Transiently express inflammasome components (GFP-NLRC4-F79A/D83A, FLAG-NAIP5, and 6myc-FlaA, all in the mscv2.2 vector backbone) via transfection with Lipofectamine 2000. The following recipe is for a single 15-cm plate; scale up accordingly. Mix 16 μg of NLRC4 plasmid, 16 μg of NAIP5 plasmid, and 8 μg of FlaA plasmid with 2 mL of Optimem. In a separate tube, mix 160 μL of Lipofectamine 2000 with 1840 μL of Optimem and incubate at room temperature for 5min. Add the diluted Lipofectamine to the plasmid mix, incubate another 20min at room temperature, and gently add the DNA—Lipofectamine mix to the 15-cm plate of HEK293T cells. Swirl to mix and incubate for 48h at 37 °C.

4. Transfection efficiency can (optionally) be assessed via GFP fluorescence, as all plasmids contain either a GFP fusion or an IRES-GFP marker in the mscv2.2 plasmid backbone. GFP fluorescence should be visible 24 h after transfection and increases in intensity thereafter.

5. 48h after transfection, harvest transfected cells by aspirating the media and incubating 5 min in 15 mL of cold PBS. Use a cell scraper to gently dislodge cells from the plate. Transfer cells to a 50-mL conical tube and pellet at $1000 \times g$ for 10min at 4 °C.

6. Prepare 25 mL of cold lysis buffer (50mM HEPES, pH 7.6; 150mM NaCl; 10mM KCl; 5mM $MgCl_2$; 5% glycerol; 1% Triton X-100; $1 \times$ protease inhibitor cocktail).

7. Prepare 500 mL of cold size exclusion buffer (50 mM HEPES, pH 7.6; 150mM NaCl; 10mM KCl; 5mM $MgCl_2$; 5% glycerol; 0.02% NP-40). Filter this buffer with a 0.2-μm filter and keep it under vacuum for 10min with occasional tapping to de-gas the buffer.

8. Prepare 1.6mL of cold elution buffer (size exclusion buffer supplemented with 0.15 mg/mL FLAG peptide).

9. Aspirate PBS from pelleted cells and resuspend in 7.5mL of cold lysis buffer. To lyse, incubate with gentle agitation or rotation for 30min at 4 °C.

10. Pellet cell debris at $16,000 \times g$ for 30min at 4 °C in micro-centrifuge.

11. Working at 4 °C, rinse chromatography column with PBS and add 200 μL of FLAG M2 agarose resin. Allow the storage buffer to drain and rinse with PBS. Add PBS as soon as buffer stops flowing to avoid drying the resin. Wash resin three times with 200 μL of 100 mM glycine, pH 3.5, letting the resin drain

completely between each wash. Wash the resin with 1 mL of PBS to remove glycine. Finally, equilibrate with 5 mL of cold lysis buffer. Cap the bottom of the chromatography column with closed stopcock.

12. Add supernatant from lysed cells to equilibrated resin. Be careful to avoid taking the cell pellet.

13. Cap the top of the chromatography column and incubate rotating at 4 °C for 2h.

14. Working at 4 °C, place chromatography column into clamp on ring stand, remove top cap, and open stopcock to allow the lysate to drain from the resin.

15. Wash the resin with 20 mL of cold size exclusion buffer, allowing resin to drain at ~1 mL/min.

16. Once the wash has completely drained, close the stopcock and add 100 μL of cold elution buffer. Incubate 3min at 4 °C before opening stopcock to collect elution fraction in a cold Eppendorf tube.

17. Repeat the elution process for a total of 8 fractions. Pool fractions 3–7 and add 1 mM DTT. FLAG resin can (optionally) be regenerated for another use by repeating the glycine washes and storing in PBS containing 0.02% sodium azide.

18. Pellet pooled eluate in micro-centrifuge at $16,000 \times g$ for 15min at 4 °C. Remove cleared eluate to fresh Eppendorf tube, being careful to avoid pelleted aggregates.

19. Working at 4 °C on the HPLC, equilibrate Superose6 size exclusion column with 1.5 column volumes of Milli-Q water followed by 1.5 column volumes of size exclusion buffer. Note that only filtered, degassed buffers should be used. The Superose6 column volume is 24 mL, and the max pressure is 1.5 MPa. Typically, this column allows only low flow rates (<0.5mL/min).

20. Using an HPLC manual injection syringe, equilibrate the 1 mL sample loop and injection port with size exclusion buffer.

21. Load cleared eluate into the injection syringe, being careful to avoid air bubbles, and then inject eluate into sample loop.

22. Using the HPLC pumps, inject sample from sample loop onto column and then elute with 1.25 column volumes of size exclusion buffer, collecting 0.5 mL fractions. Follow the elution of inflammasome complexes via UV absorbance at 280 nm. Note that large protein complexes enter resin poorly and are eluted faster than individual protein components. Assembled inflammasomes should elute beginning at ~0.35 column volumes, whereas unassembled components will elute much later.

23. Add 20% trehalose to the peak elution fraction and use for cryo-EM analysis. Store the sample on ice and prepare grids as soon as possible as described in the protocol in Section 4.2. If the sample must be stored, immediately flash-freeze small aliquots in liquid nitrogen and keep at −80 °C.

4.   Preparation of cryo-EM grids

As with most samples being prepared for cryo-EM analysis, an initial assessment of the biochemical preparation's potential can be conducted using negatively stained EM techniques. Less concentrated samples can generally be used for negatively stained EM grid preparation than can be used for cryo-EM grid preparation, and compared to screening cryo-EM grids, checking negatively stained EM grids is fast and simple. Although these negatively stained samples will not give rise to high-resolution structures, preparing them is worthwhile. A sample that has noticeable impurities or does not appear concentrated enough in negatively stained EM will almost certainly not look better in cryo-EM. Once a sample looks free of such problems in negatively stained EM, screening for optimal cryo-EM grid preparation conditions can begin.

With some samples, including the NAIP5–NLRC4 inflammasomes as we prepared them, one does not have the luxury of finding the right cryo-EM parameters through brute-force screening of dozens of conditions, particularly since these inflammasomes are time-consuming to prepare. In our experience, inflammasomes are delicate (i.e., they cannot be repeatedly flash-frozen and thawed, and even one round of freezing and thawing is not optimal), and it is essential that consideration is devoted to selecting grid preparation parameters that are likely to yield grids suitable for data collection.

Some groups using cryo-EM to study NAIP–NLRC4 inflammasomes have used conventional grid preparation methods. However, their preparations have been different from ours in several ways, using methods such as blocking full inflammasome formation (mutating the NLRC4 "donor" surface to prevent large rings from assembling) and deleting the NLRC4 CARD. We did not use these methods (see Section 3.1, for more information) and encountered difficulties preparing our inflammasome grids conventionally. In this section, we share how we overcame two major problems—that of missing side views and that of low particle density—using easily fabricated tools. The technique we describe may be useful for preparing other, unrelated complexes as well. We also provide our full protocol for preparing NAIP–NLRC4 cryo-EM grids.

4.1   Minimizing preferred orientations and increasing particle density

One of the first difficulties we encountered when preparing NAIP5–NLRC4 inflammasome grids is a common one: low particle density. When it is not possible to further concentrate a sample prior to grid application or when increasing concentration does not sufficiently increase the particle density seen on the grid, as in our case, the electron microscopist has many options. Often, applying a supporting layer of continuous carbon to the cryo-EM grid and glow discharging the grid just prior to sample application increases particle density. We found this to be necessary with our NAIP5–NLRC4 inflammasome samples, but it was not until we introduced our new technique that we were able to increase particle density sufficiently to make 3D reconstruction practical.

We originally conceived of this technique to solve a second problem familiar to cryo-electron microscopists: preferred orientations. We saw many circular top views of the NAIP5–NLRC4 inflammasome in our micrographs, but relatively few of the crescent-shaped

side views, particularly in micrographs from cryo-EM grids rather than micrographs from negatively stained EM grids. Inflammasomes are roughly disk-shaped complexes and much longer in one dimension than the other, so we hypothesized that contact with the air–water interface during the longer sample application time required to reach high particle density on the grid for cryo-EM was causing inflammasomes that were originally in the side-view orientation to rotate toward a top-view orientation—or to denature, since we did observe denatured particles in micrographs from many cryo-EM grids.

Incubating our inflammasomes on grids in a humidity chamber, as is often done when samples must be incubated on cryo-EM grids for long periods of time (on the order of minutes), was not sufficient to prevent this problem. Thus, we developed a simple apparatus we call the grid floater. The experimental setup contains both the grid floater and a Teflon well plate, a machined piece of Teflon with smooth holes drilled into it to serve as wells for liquid samples (see Fig. 1). Teflon was our material of choice because it is easy to work with, inexpensive, and not prone to reacting with the biological material or accumulating residues. In our protocol, a small volume (~20 μL) of prepared inflammasome samples is aliquoted into a Teflon well, forming a droplet with a meniscus high above the Teflon. The grid is then rested (or "floated"), carbon-side down, on the droplet for incubation. With experience, some particularly dexterous individuals may be able to capture the grid with tweezers when the time for plunge-freezing comes, but we preferred to use the grid floater, which could be any device that allows a pair of tweezers pre-loaded with a grid to be aligned precisely atop the sample droplet. Using the grid floater ensures that the grid will be gripped perfectly by the rim every time. In practice, we used a ramp-shaped object made of many layers of crumpled aluminum foil as our grid floater (see Fig. 2). This inexpensive, improvised device proved easily adjustable by bending to accommodate different droplet heights (which vary due to volume dispensed, surface tension, etc.) as well as durable. Clearly, though, many other objects could be used as support for the tweezers.

After incubating the sample on the grid, we rinsed the surface of the grid for 10 s by gently touching it, sample side down, to a 20-μL droplet of EM washing buffer (see Section 4.2, for recipe) contained in another well. The main purpose of this step is to reduce the concentration of glycerol, which is present at 5% in the size exclusion buffer (see Section 3.3.3, for recipe), replacing it with a small amount of trehalose. Both glycerol and trehalose are cryoprotectants, but glycerol reduces contrast in the images more than trehalose does, so it is desirable to remove at least some of the glycerol. Since rinsing leaves some residual glycerol, we tried rinsing with up to three droplets of buffer of up to 30 μL each, but this did not appear to improve contrast compared to using just one smaller droplet.

Using the grid floater just described, the particles adhering to the grid are most at risk of coming into contact with the air–water interface during the moment it takes to blot and plunge-freeze the grid. Of course, it is important not to blot excessively at this stage, recalling that the vitreous ice must be thick enough to still contain particles in the side-view orientation. Those who have experience blotting and plunge-freezing by hand will find that it is easy to do so using this setup, although we did use a Vitrobot in our studies.

We found that using this grid floater, the preferred orientation problem was much reduced, although still not totally eliminated, and since we were able to incubate our samples on the grids longer without worrying about evaporation of the droplet, we were able to increase the number of particles on the grid as well. (Note that no further improvement in particle density was seen after 10–15 min of incubation.) This setup could thus be useful for any samples requiring prolonged incubation times on cryo-EM grids.

It should be mentioned that there are alternatives to using the grid floater that may also increase particle number and/or reduce the preferred orientation problem, although they may not be as simple or inexpensive. Namely, using grid coatings such as streptavidin monolayers (with compatible biotinylated samples) and graphene or graphene derivatives, to name just two types, may be worth exploring (Han et al., 2016; Hu et al., 2015; Palovcak et al., 2018; Russo & Passmore, 2014, 2016; Wang, Ounjai, & Sigworth, 2008). For the most part, these alternative methods should not be incompatible with grid floating, and we encourage those working with difficult samples to try them in combination.

4.2   Protocol for NAIP5–NLRC4 inflammasome cryo-EM grid preparation

4.2.1   Equipment

- 0.2 μm filter

- Grid floater (see Section 4.1)

- Teflon well plate stored in Milli-Q water (see Section 4.1)

- Micropipettes

- C-flat holey carbon grids (Protochips) with thin layer of amorphous carbon deposited as described by Passmore and Russo (2016)

- Solarus Plasma Cleaner (Gatan)

- Vitrobot Mark II (FEI) or other plunge-freezing apparatus for cryo-EM, including tweezers

- Cryo-EM grid boxes

- Aluminum foil

- Ultrasonic bath sonicator

- Glass beaker large enough to store Teflon well plate

4.2.2   Materials

- Milli-Q water

- HEPES, pH 7.6

- NaCl

- KCl

- $MgCl_2$

- Trehalose

- NP-40

- Nitrogen gas

- Dry liquid nitrogen

- 100% ethanol

- ES 7 × cleaning solution

4.2.3 Protocol

1. Prepare EM washing buffer (50mM HEPES, pH 7.6, 150mM NaCl, 10mM KCl, 5mM $MgCl_2$,1%trehalose, 0.02% NP-40). Do not shake or vortex mix after adding NP-40. Slowly pass through a 0.2-μm filter. EM washing buffer without trehalose and NP-40 may be prepared in advance and stored, but the trehalose and NP-40 must be added just prior to use.

2. Remove Teflon well plate from Milli-Q water and dry with nitrogen gas. Using a micropipette, rinse all wells to be used with EM washing buffer.

3. Test the height and alignment of the grid floater by adding a droplet of EM washing buffer to one of the wells in the Teflon well plate and positioning the tip of the Vitrobot tweezers over the droplet. Ensure that a grid held by the tweezers would rest atop the droplet.

4. Plasma clean grids 8s in air using a Solarus Plasma Cleaner (Gatan) operated at 10 W.

5. Set up Vitrobot according to manufacturer's instructions at 22 °C and 100% relative humidity.

6. Add 20 μL droplet of inflammasomes (prepared as described in Section 3.3.3) and 20 μL droplet of EM washing buffer to separate wells in the Teflon well plate.

7. Grip one of the plasma-cleaned grids by the edge using Vitrobot tweezers and place it, carbon-side down, on the droplet of inflammasomes. Incubate for 10min.

8. Use the tweezers to remove the grid from the inflammasome droplet, then immediately rinse the grid by gently touching the sample side to the droplet of EM buffer for 10s. Do not submerge the grid or otherwise allow buffer to come in contact with the back of the grid.

9. Immediately load the tweezers on the Vitrobot and plunge-freeze the grid in liquid ethane with no delay between blotting and freezing. Store the grids in plastic cryo-EM grid boxes in dry liquid nitrogen until use.

10. Clean and store Teflon well plate. To clean, soak overnight in 1% *v*/v ES 7 × cleaning solution diluted in Milli-Q water (or other dilute, phosphate-free detergent), then rinse the plate 20 times with Milli-Q water. Ensure that cleaning

solution and water enter all the wells. Submerge well plate in 100% ethanol in a glass beaker, ensure ethanol enters all wells, cover the beaker with aluminum foil, and sonicate in an ultrasonic bath sonicator for 30min. Rinse the plate 20 more times with Milli-Q water and store fully submerged in Milli-Q in a beaker covered with aluminum foil. Ensure that water fills all wells before storage.

5. Cryo-EM data collection and analysis

Even after undertaking diligent work in preparing and screening samples, care is required during data collection and processing. The cryo-EM data collection and processing pipeline we used for the NAIP5–NLRC4 inflammasome (Fig. 3) is similar in many respects to that used for most asymmetric biological samples. First, micrographs that are good—a judgment based on criteria such as having an abundance of intact particles in many views and lacking ice contamination—are selected for use. Particles are then picked from these micrographs by hand or using software, and various preprocessing steps, such as corrections for contrast transfer function and drift, are conducted. Two-dimensional (2D) classification is often used at this stage to remove particles that do not align with others and for initial analysis. Next, particles are typically further sorted into three-dimensional (3D) classes, and the class(es) deemed biologically relevant and likely to yield high-resolution reconstructions are refined and further polished. Finally, depending on resolution and other factors, various types of structural modeling may also be done.

Some aspects of this process are typically consistent from sample to sample, but there are many additional considerations for each case. In this section, we focus on the specific strategies we used for the NAIP5–NLRC4 inflammasome that we believe may be useful to others studying it in the future. Some of these methods may also be useful for dealing with other samples sharing similar issues, such as preferred views and severe compositional and conformational heterogeneity. We do not aim to provide a full guide to the standard cryo-EM methods we employed, which have been extensively described in other texts referenced throughout this chapter.

5.1 Data collection

Given the relatively high resolutions of currently available structures of NAIP–NLRC4 inflammasomes and their components, those seeking new structures should undoubtedly plan to use a microscope equipped with a direct electron detector. The use of these detectors has revolutionized structural biology over the past several years, making it possible to use cryo-EM to solve structures of biological macromolecules at unprecedentedly high resolution (Passmore & Russo, 2016).

Electron microscopes and the software used to operate them have also become much more advanced in recent years, and many steps that until recently vexed researchers can now be done automatically. Even the newest electron microscopes with the highest level of automation, however, should not be left to run unsupervised for prolonged periods if a data collection session is to be successful, especially when working with difficult samples. During data collection, it is essential to consistently assess whether micrographs being

collected are suitable for use and to adjust the microscope or change to new areas of the grid accordingly.

For the NAIP5–NLRC4 inflammasome and other samples that exhibit preferred orientations, a special consideration is whether the underrepresented views (in this case, side views) are present. If not, in the case of these inflammasomes, it is likely necessary to move to an area with thicker ice to see all views. To limit the resolution-diminishing impact of greater ice thickness, choose the grid areas with the thinnest ice that contains side views (see Fig. 3A for a micrograph from an optimal grid area). Note that to best visualize particles in thicker ice, the defocus may need to be higher magnitude than is typically used for cryo-EM; we used a range of –1.8 μm through –4.0 μm. Using a phase plate and/or energy filter (if available) may alleviate this problem, but we did not have a chance to experiment with either for our work.

To truly maximize the potential of a microscope session, when possible, one should initiate some on-the-fly, preliminary data processing as each micrograph is collected. Early-stage processing (e.g., particle picking and contrast transfer function estimation) can now be conducted rapidly with GPU-based programs such as Gautomatch and Gctf (Zhang, 2016; Zhang & Zhang, n.d.). A new GPU-based program, Warp, offers another option for quick preprocessing (Tegunov & Cramer, 2018). Even programs capable of 2D and 3D classification and refinement, including CryoSPARC and RELION, can now be run on GPUs and provide feedback on the quality of data as it is being collected (Kimanius, Forsberg, Scheres, & Lindahl, 2016; Punjani, Rubinstein, Fleet, & Brubaker, 2017).

5.2 Micrograph selection and particle picking

Although options exist for automatic micrograph selection, it is our experience that it is well worth the time to check each micrograph manually. The usual considerations, such as avoiding micrographs with excessive ice contamination or drift that cannot be adequately corrected, apply to the NAIP–NLRC4 inflammasomes. However, there are some additional characteristics to note about micrographs of these complexes.

During data collection, the microscopist should have attempted to find grid areas that have ice just thick enough to support side views (see Section 5.1). Some images from these areas may have ice that is too thick to produce high-resolution reconstructions; these images will appear dimmer and the particles will not seem as crisp. (Be sure to adjust display contrast and brightness to avoid throwing away potentially useful micrographs.) Other images from areas directly adjacent to ideal ones may suffer the opposite problem: the ice may be slightly too thin, resulting in images with few side views—or, at worst, images containing many damaged particles that appear fuzzy or distorted. These micrographs should also be discarded.

Particle picking is another process with many options for full automation. With the NAIP5–NLRC4 inflammasome, automatic picking may be sufficient for real-time assessment of data quality during a session. However, for this sample, we found that the best option when seeking high resolution is to pick particles manually or to use manual picking to generate 2D class averages equally representing all views of the complex and to use these class averages

as templates for automatic picking. This is because the side views resemble the top views so little that non-template-based automatic picking methods can often be made to select either side or top views, but not both. We tried RELION and FindEM for template-based picking, with comparable results (Roseman, 2004; Scheres, 2012).

At minimum, if automatic picking is used, particle picks from several micrographs of various defocus values from different grid areas should be examined to ensure few to no good particles are missed while undesirable particles (such those that appear "exploded" or indistinct) and non-particles are not selected. Inspecting micrographs and picked particle can even be combined: using RELION, one can easily open micrographs, add or remove particle picks, and discard any micrographs that are not of acceptable quality using the graphical user interface.

5.3 Sorting particles in 2D and 3D

Methods for sorting particles after extracting them from micrographs are as varied as the samples to which they are applied. In most cases, 2D classification is done after particle extraction and preprocessing. In principle, 3D classification can be done without classifying in two dimensions first, but in our case including the preliminary 2D step led to better results.

2D classification can yield interesting results on its own. For example, we observed early on that NAIP5–NLRC4 inflammasomes vary in the number of subunits they contain. 2D results can also be used as an indicator of the potential of a dataset. For the NAIP5–NLRC4 inflammasome, for instance, the number of particles going into each 2D class is of interest—if there is a dearth of side views at this stage, it should not come as a surprise if the 3D reconstruction is of low quality or exhibits strong resolution anisotropy. Also, if 2D class averaging yields classes in which internal structural details such as alpha helices can be seen, it is more likely that the data contains enough high-resolution information to generate a top-quality reconstruction. (As with micrograph inspection, it may be necessary to adjust display contrast and brightness when checking 2D classes for these details.) Often, particles sorted into 2D classes that appear hazy or do not resemble the sample of interest are discarded at this stage; we did this with our NAIP5–NLRC4 inflammasome data (see Fig. 3B).

The standard next step, 3D class averaging, is a stage of processing that allows the user considerable flexibility and can make the difference between solving a high-resolution structure and achieving nothing. (Note that in this section we generally refer to 3D classification practices in RELION and CryoSPARC, the two programs of which we made the most use). Hypothetically, one could proceed directly to 3D refinement using all particles, but conducting 3D classification first offers an opportunity not only to rid the dataset of more of low-quality (junk) particles, but also to sort out heterogeneity and sometimes even to glean some insights into the biology. For example, in the case of our NAIP5–NLRC4 inflammasome data, we immediately observed that, no matter what processing parameters we used, each "non-junk" class consisted of an open ring of identical-looking subunits nucleated by a single larger subunit. The smaller subunits were later

confirmed to be NLRC4 monomers, whereas the larger subunit was NAIP5 bound to flagellin.

It is always prudent to try 3D classification using a variety of parameters. Varying the number of classes, for instance, sometimes yields dramatically different results. With too few classes, junk may not be sorted out, and if the sample is heterogeneous, dissimilar particles will be forced into classes with each other. With too many classes, particles that do not actually represent different states may be sorted apart from one another, resulting in a lower particle number available for refinement and sometimes, thus, a final reconstruction of lower resolution. It is therefore critical to attempt the process several times, with different parameters, and ideally with more than one program to see which yields the best results after the most promising classes (i.e., those that achieve the highest resolution in the areas of interest) are refined.

Due to heterogeneity, the 3D classification process is especially important when working with NAIP5–NLRC4 inflammasomes. It may be worthwhile to select the best classes from the first round of three-dimensional classification and subject those classes to further rounds of classification. This strategy did not yield any reconstructions with higher resolution in our case, possibly because of dwindling particle numbers as the classification process went on— with a greater starting number of particles, the results may have been better. However, the process did help confirm our suspicions that these inflammasomes exist in a variety of states, varying especially in the number of NLRC4 subunits each ring contains (see Fig. 3D).

We also noticed that in no case did we find 3D classes in which the inflammasome rings fully closed, with NLRC4's donor surface contacting NAIP5—rather, the inflammasomes appeared to twist into short helices, a finding supported but not conclusively shown by some further structural modeling our group conducted. This finding was not central to our results; nevertheless, it is in alignment with some other observations and may have functional implications (Diebolder, Halff, Koster, Huizinga, & Koning, 2015; Li et al., 2018; Matyszewski et al., 2018). Thus, extensive three-dimensional classification can provide biological insights, even when the result is not a high-resolution structure—although, of course, that is usually one of the goals of any structural study.

5.4 Refinement and modeling

Once a 3D class of interest has been selected, 3D refinement of particles from the class is needed to produce a structure with the highest resolution possible. As with 3D classification, it is advisable to run the refinement several times using different parameters, as the results may vary substantially in quality. Overall resolution may vary from refinement to refinement as parameters are manipulated, and local resolution should also be checked—we paid closest attention to refinements that had the best local resolution in areas we believed to be most biologically relevant, such as the interface between NAIP5 and flagellin.

It is advisable to check for resolution anisotropy (better resolution in one direction than another) at this stage and, if it is observed, to determine whether it is present to such a degree that it would hinder any further analysis. If resolution anisotropy is beyond a manageable level, first ensure that side views are not being accidentally discarded during

sorting (see Section 5.3). On this issue, a useful diagnostic is to run 2D class averaging on the particles that went into the 3D refinement in question and check whether the proportion of side views is on par with that of the entire dataset. If the proportion of side views is much lower in the set of particles going into the refinement, redoing the 3D classification with different parameters may help. If the proportion of side views was very low from the beginning, as seen in the original 2D class averages, more data may need to be collected and pooled with the existing dataset to ameliorate the resolution anisotropy. To minimize the additional labor and risk of error when collecting additional data to pool with the first dataset, it is easiest to use the same data collection parameters (e.g., pixel size) each time.

Optimally, the data to be added would come from grids with a greater proportion of side views. But even if all conceivable means to increase the proportion of side views have already been explored (see Section 4.1, for our solutions), increasing the absolute number of side views simply by collecting more data may still improve overall resolution and reduce or resolve anisotropy as the improvements in resolution in one direction from greater and greater numbers of top views come to a halt. We found this to be the case with the number of particles used throughout our analysis (under one million), although this brute-force method may not be seen as the optimal way to make use of microscope time if there is concurrently the problem of low number of particles per micrograph (see Section 4.1, for our suggested solution to that issue). After collecting this additional data, there was no noticeable resolution anisotropy in our final reconstructions, despite the fact that we were not able to totally eliminate the problem of preferred orientations.

It is also a good idea to try the refinement in more than one program. We obtained results of similar resolution using RELION and CryoSPARC, but RELION provided more useful results because, at the time of our work, RELION but not CryoSPARC offered masked local refinement. Thus, using RELION, one could focus the refinement on the region of greatest interest. In the case of the NAIP5–NLRC4 inflammasome structure, we made extensive use of masking. Since the particles varied in the number of NLRC4 subunits they contained, we found (as would be expected) areas of much lower resolution farther from the nucleation point of the ring due to variable occupancy.

For this reason, we applied a mask around the region containing only NAIP5, flagellin, and the first two NLRC4 subunits at the start of local searches during refinement in RELION. The rationale for using a mask around this particular region was that we could capture the structures of all three unique components of the NAIP5–NLRC4 inflammasome as well as all the possible interfaces (NAIP5–flagellin, NAIP5–NLRC4, and NLRC4–NLRC4) while ignoring the most heterogeneous areas. This allowed us to pool particles from classes that had different numbers of NLRC4 subunits, increasing our final resolution. We also attempted locally masked refinement with different numbers of subunits, without the flexible portion of flagellin, and without the CARDs, as well as masking during 3D classification, but did not achieve better results. To generate masks, we segmented the areas of interest from the full EM density of the inflammasome in Chimera and saved them separately, then used them as inputs for RELION's automatic mask generation tool with varying parameters (Pettersen et al., 2004; Scheres, 2012). We ran refinements and classifications with masks of varying tightness before discovering the one that worked best in our case. Now that local

masking during refinement is an option in CryoSPARC, it would be interesting to apply the program to our data again.

It is worth noting that even when masked local refinement is not done, choice of the overall mask used during refinement can make a great difference in the resolution of the resulting structure. A too-tight mask that cuts into the density can lead to falsely inflated calculated resolution, whereas one that is too loose may result in resolution that is lower than could be achieved with an optimal mask. Thus, it is generally worth experimenting with different masks during refinement, regardless of the sample and regardless of whether locally masked refinement is being done.

Once refinement and any postprocessing are complete, the choice of structural modeling methods depends on a multitude of factors, perhaps most important of which is resolution. Resolution dictates whether a model can be built into the EM density de novo, for example, and has a major impact on how confident one can be in a model. Since the resolution of our NAIP5–NLRC4 inflammasome structure varied widely from region to region, we filtered the structure by local resolution, using different modeling methods in different areas. We refer any readers interested in our full modeling methods to our recent paper, where they are described in extensive detail (Tenthorey et al., 2017). However, it is our hope that future researchers studying these inflammasomes will improve on the resolution we achieved, necessitating different modeling techniques, a full explanation of which is well beyond the scope of this chapter.

6.   Concluding remarks

Despite the existence of some published structures, our understanding of inflammasome structures and their functional implications remains far from complete. We hope that the methods described in this chapter will help others step beyond the frontiers of our current knowledge by increasing the resolution of existing structures and by investigating other states, such as the caspase-1-bound inflammasome. We also hope this chapter will find its way into the hands of researchers struggling with other difficult samples and serve as a starting point to guide their studies.

Acknowledgments

References

Aglietti RA, Estevez A, Gupta A, Ramirez MG, Liu PS, Kayagaki N, et al. (2016). GsdmD p30 elicited by caspase-11 during pyroptosis forms pores in membranes. Proceedings of the National Academy of Sciences of the United States of America, 113, 7858–7863. 10.1073/pnas.1607769113. [PubMed: 27339137]

Bergsbaken T, Fink SL,& Cookson BT (2009). Pyroptosis: Host cell death and inflammation. Nature Reviews. Microbiology, 7, 99. [PubMed: 19148178]

Broz P, & Dixit VM (2016). Inflammasomes: Mechanism of assembly, regulation and signalling. Nature Reviews. Immunology, 16, 407–420.

Chen X, He W-T, Hu L, Li J, Fang Y, Wang X, et al. (2016). Pyroptosis is driven by non-selective gasdermin-D pore and its morphology is different from MLKL channel-mediated necroptosis. Cell Research, 26, 1007–1020. 10.1038/cr.2016.100. [PubMed: 27573174]

Diebolder CA, Halff EF, Koster AJ, Huizinga EG, & Koning RI (2015). Cryoelectron tomography of the NAIP5/NLRC4 inflammasome: Implications for NLR activation. Structure, 23, 2349–2357. 10.1016/j.str.2015.10.001. [PubMed: 26585513]

Ding J, Wang K, Liu W, She Y, Sun Q, Shi J, et al. (2016). Pore-forming activity and structural autoinhibition of the gasdermin family. Nature, 535, 111. [PubMed: 27281216]

Han B-G, Watson Z, Kang H, Pulk A, Downing KH, Cate J, et al. (2016). Long shelf-life streptavidin support-films suitable for electron microscopy of biological macromolecules. Journal of Structural Biology, 195, 238–244. 10.1016/j.jsb.2016.06.009. [PubMed: 27320699]

Hu Z, Yan C, Liu P, Huang Z, Ma R, Zhang C, et al. (2013). Crystal structure of NLRC4 reveals its autoinhibition mechanism. Science, 341, 172–175. [PubMed: 23765277]

Hu Z, Zhou Q, Zhang C, Fan S, Cheng W, Zhao Y, et al. (2015). Structural and biochemical basis for induced self-propagation of NLRC4. Science, 350, 399–404. [PubMed: 26449475]

Jones JDG, Vance RE, & Dangl JL (2016). Intracellular innate immune surveillance devices in plants and animals. Science, 354, aaf6395–1–aaf6395–8. [PubMed: 27934708]

Kimanius D, Forsberg BO, Scheres SHW, & Lindahl E (2016). Accelerated cryo-EM structure determination with parallelisation using GPUs in RELION-2. eLife, 5, e18722 10.7554/eLife. 18722. [PubMed: 27845625]

Kofoed EM, & Vance RE (2011). Innate immune recognition of bacterial ligands by NAIPs dictates inflammasome specificity. Nature, 477, 592–595. 10.1038/nature10394. [PubMed: 21874021]

Li Y, Fu T-M, Lu A, Witt K, Ruan J, Shen C, et al. (2018). Cryo-EM structures of ASC and NLRC4 CARD filaments reveal a unified mechanism of nucleation and activation of caspase-1. Proceedings of the National Academy of Sciences of the United States of America, 115, 10845–10852. 10.1073/pnas.1810524115. [PubMed: 30279182]

Liu X, Zhang Z, Ruan J, Pan Y, Magupalli VG, Wu H, et al. (2016). Inflammasome-activated gasdermin D causes pyroptosis by forming membrane pores. Nature, 535, 153. [PubMed: 27383986]

Lu A, Li Y, Schmidt FI, Yin Q, Chen S, Fu T-M, et al. (2016). Molecular basis of caspase-1 polymerization and its inhibition by a new capping mechanism. Nature Structural & Molecular Biology, 23, 416–425. 10.1038/nsmb.3199.

Martinon F, Burns K, & Tschopp J (2002). The Inflammasome: A molecular platform triggering activation of inflammatory caspases and processing of proIL-β. Molecular Cell, 10, 417–426. 10.1016/S1097-2765(02)00599-3. [PubMed: 12191486]

Matyszewski M, Zheng W, Lueck J, Antiochos B, Egelman EH, & Sohn J (2018). Cryo-EM structure of the NLRC4^{CARD} filament provides insights into how symmetric and asymmetric supramolecular structures drive inflammasome assembly. Journal of Biological Chemistry, 293, 20240–20248. 10.1074/jbc.RA118.006050. [PubMed: 30385506]

Palovcak E, Wang F, Zheng SQ, Yu Z, Li S, Betegon M, et al. (2018). A simple and robust procedure for preparing graphene-oxide cryo-EM grids. Journal of Structural Biology, 204, 80–84. 10.1016/j-jsb.2018.07.007. [PubMed: 30017701]

Passmore LA, & Russo CJ (2016). Specimen preparation for high-resolution cryo-EM. Methods in Enzymology, 579, 51–86. 10.1016/bs.mie.2016.04.011. [PubMed: 27572723]

Pettersen EF, Goddard TD, Huang CC, Couch GS, Greenblatt DM, Meng EC, et al. (2004). UCSF chimera—A visualization system for exploratory research and analysis. Journal of Computational Chemistry, 25, 1605–1612. 10.1002/jcc.20084. [PubMed: 15264254]

Punjani A, Rubinstein JL, Fleet DJ, & Brubaker MA (2017). cryoSPARC: Algorithms for rapid unsupervised cryo-EM structure determination. Nature Methods, 14, 290. [PubMed: 28165473]

Rayamajhi M, Zak DE, Chavarria-Smith J, Vance RE, & Miao EA (2013). Mouse NAIP1 detects the type III secretion system needle protein. Journal of Immunology (Baltimore, Md. : 1950), 191, 3986–3989. 10.4049/jimmunol.1301549.

Roseman AM (2004). FindEM—A fast, efficient program for automatic selection of particles from electron micrographs. Journal of Structural Biology, 145, 91–99. 10.1016/j.jsb.2003.11.007. [PubMed: 15065677]

Ruan J, Xia S, Liu X, Lieberman J, & Wu H (2018). Cryo-EM structure of the gasdermin A3 membrane pore. Nature, 557, 62–67. 10.1038/s41586-018-0058-6. [PubMed: 29695864]

Russo CJ, & Passmore LA (2014). Controlling protein adsorption on graphene for cryo-EM using low-energy hydrogen plasmas. Nature Methods, 11, 649. [PubMed: 24747813]

Russo CJ, & Passmore LA (2016). Progress towards an optimal specimen support for electron cryomicroscopy. Current Opinion in Structural Biology, 37, 81–89. 10.1016/j.sbi.2015.12.007. [PubMed: 26774849]

Sborgi L, Rühl S, Mulvihill E, Pipercevic J, Heilig R, Stahlberg H, et al. (2016). GSDMD membrane pore formation constitutes the mechanism of pyroptotic cell death. The EMBO Journal, 35, 1766–1778. 10.15252/embj.201694696. [PubMed: 27418190]

Scheres SHW (2012). RELION: Implementation of a Bayesian approach to cryo-EM structure determination. Journal of Structural Biology, 180, 519–530. 10.1016/j.jsb.2012.09.006. [PubMed: 23000701]

Shi Y (2004). Caspase activation: Revisiting the induced proximity model. Cell, 117, 855–858. 10.1016/j.cell.2004.06.007. [PubMed: 15210107]

Tegunov D, & Cramer P (2018). Real-time cryo-EM data pre-processing with warp. bioRxiv. 338558 10.1101/338558.

Tenthorey JL, Haloupek N, LóSpez-Blanco JR, Grob P, Adamson E, Hartenian E, et al. (2017). The structural basis of flagellin detection by NAIP5: A strategy to limit pathogen immune evasion. Science, 358, 888–893. [PubMed: 29146805]

Wang L, Ounjai P, & Sigworth FJ (2008). Streptavidin crystals as nanostructured supports and image-calibration references for cryo-EM data collection. Journal of Structural Biology, 164, 190–198. 10.1016/j-jsb.2008.07.008. [PubMed: 18707004]

Yang X, Yang F, Wang W, Lin G, Hu Z, Han Z, et al. (2017). Structural basis for specific flagellin recognition by the NLR protein NAIP5. Cell Research, 28, 35. [PubMed: 29182158]

Yang J, Zhao Y, Shi J, & Shao F (2013). Human NAIP and mouse NAIP1 recognize bacterial type III secretion needle protein for inflammasome activation. Proceedings of the National Academy of Sciences of the United States of America, 110, 14408–14413. 10.1073/pnas.1306376110. [PubMed: 23940371]

Zhang K (2016). Gctf: Real-time CTF determination and correction. Journal of Structural Biology, 193, 1–12. 10.1016/j-jsb.2015.11.003. [PubMed: 26592709]

Zhang J. (Kai), Zhang. (n.d.). Jack (Kai) http://www.mrc-lmb.cam.ac.uk/kzhang/, Accessed 8 May 2019.

Zhao Y, Yang J, Shi J, Gong Y-N, Lu Q, Xu H, et al. (2011). The NLRC4 inflammasome receptors for bacterial flagellin and type III secretion apparatus. Nature, 477, 596–600. [PubMed: 21918512]
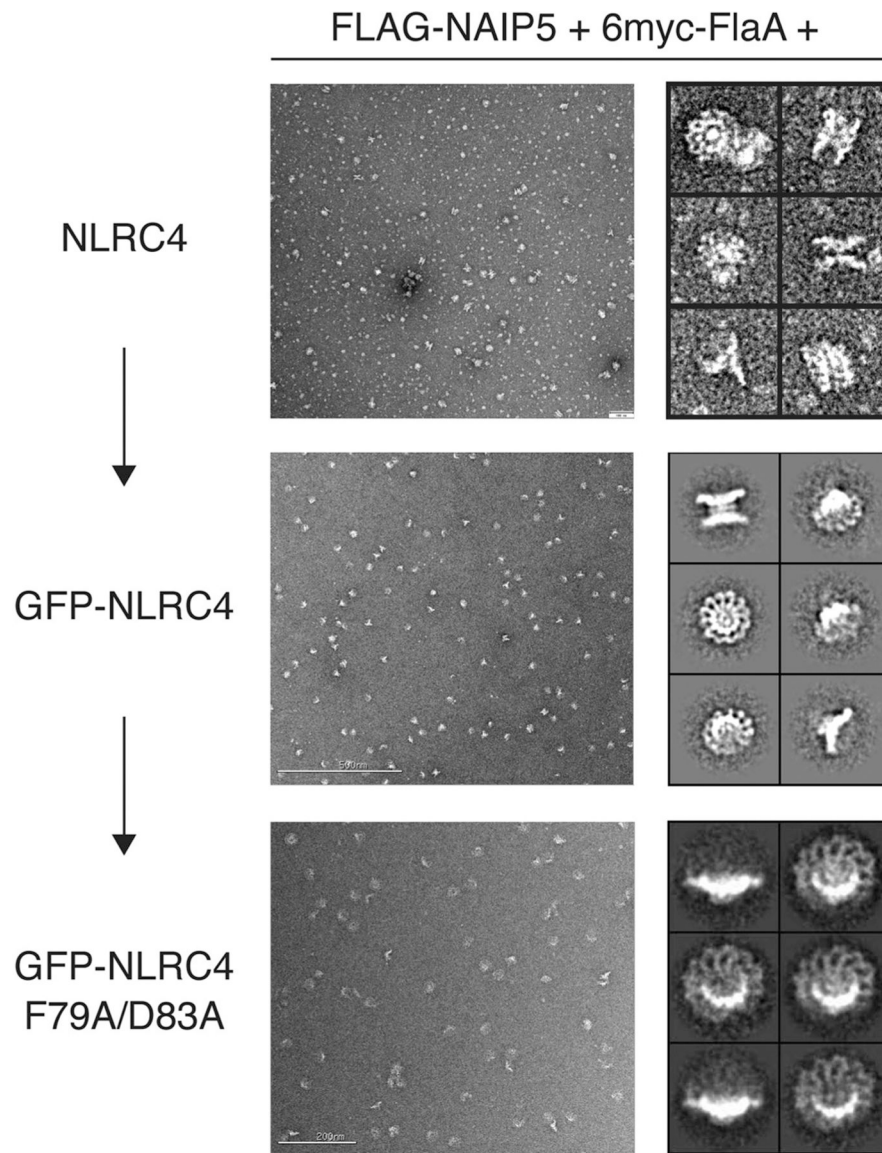
Fig. 1.

Biochemical optimization. Micrographs of negatively stained NAIP5–NLRC4 inflammasomes (left) and 2D class averages (right) reveal the presence of stacked rings. Only when two CARD mutations and an N-terminal GFP tag are added to NLRC4 (bottom) is ring stacking reduced to a manageable level. See Section 3.1 for more information. *Part of this figure is reused with publisher's permission from Tenthorey, J. L., Haloupek, N., López-Blanco, J.R., Grob, P., Adamson, E., Hartenian, E., et al. (2017). The structural basis of flagellin detection by NAIP5: A strategy to limit pathogen immune evasion. Science, 358, 888–893.*
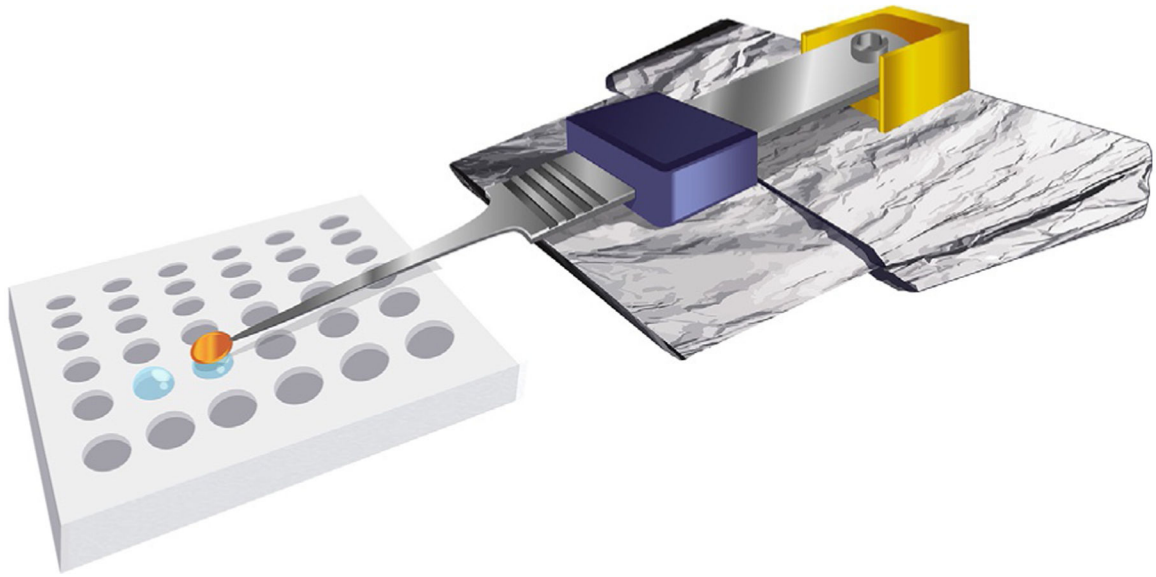
Fig. 2.
Depiction of the grid floater and Teflon well plate in use. The edge of the EM grid is gripped by Vitrobot tweezers and rests, carbon-side down, on a sample droplet. After incubation, the downward-facing surface of the grid is gently rinsed in the second droplet, which contains only buffer, and then the tweezers are loaded in the Vitrobot. See Section 4.2 for the full protocol.
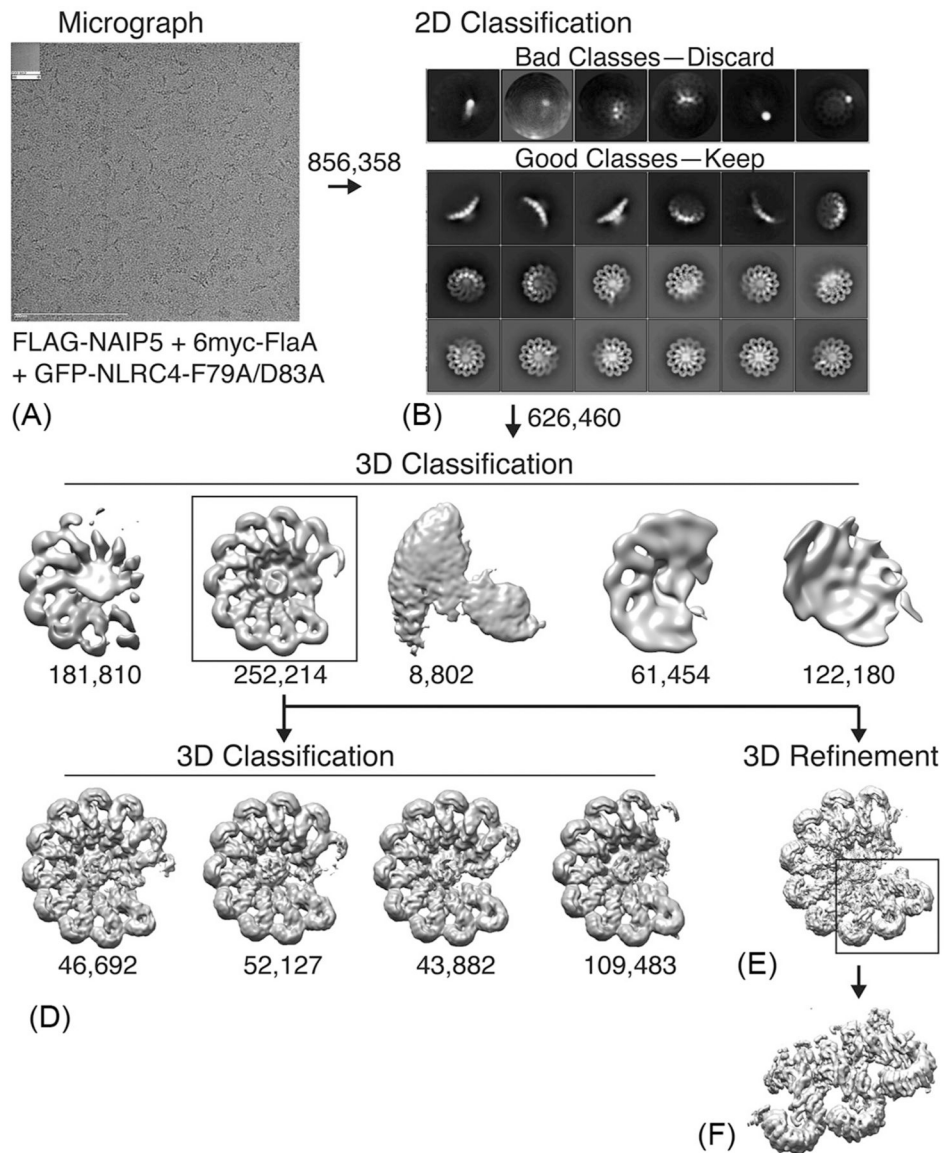
Fig. 3.
Data processing pipeline leading to the reconstruction of the NAIP5–NLRC4 inflammasome in Tenthorey et al. Numbers in this figure refer to numbers of particles. (A) A representative micrograph. Note the presence of both crescent-shaped side views and circular top views. (B) Representative 2D class averages. Particles in bad classes—those that were blurry and/or did not resemble particles—were discarded at this stage. (C) The results of RELION's 3D classification into five classes. This step yielded only one class (boxed) with potential for producing a high-resolution structure. (D) The results of further 3D classification of the best 3D class from (C). This classification step mainly sorted particles on the basis of number of NLRC4 subunits. Further refinement of any of these classes did not yield better results than refinement of the pooled classes shown in (E). (F) The result of focused refinement of NAIP5, flagellin, and the first two NLRC4 subunits using the same particles used in (E). For full details on the data processing, including the rationale behind each step, see Section 5.

This figure is reused with publisher's permission from Tenthorey, J. L., Haloupek, N., López-Blanco, J.R., Grob, P., Adamson, E., Hartenian, E., et al. (2017). The structural basis of flagellin detection by NAIP5: A strategy to limit pathogen immune evasion. Science, *358, 888–893.*